

A multi-wavelength investigation of the non-thermal radio emitting O-star 9 Sgr[★]

G. Rauw^{1,★★}, R. Blomme², W. L. Waldron³, M. F. Corcoran⁴, J. M. Pittard⁵, A. M. T. Pollock^{6,7}, M. C. Runacres², H. Sana^{1,★★★}, I. R. Stevens⁸, and S. Van Loo²

¹ Institut d’Astrophysique, Université de Liège, Allée du 6 Août, Bât. B5c, 4000 Liège (Sart Tilman), Belgium

² Royal Observatory of Belgium, Avenue Circulaire 3, 1180 Brussels, Belgium

³ L-3 Communications Analytics Corporation, 1801 McCormick Drive, Suite 170, Largo, MD 20774, USA

⁴ USRA/HEASARC Goddard Space Flight Center, Greenbelt, MD 20771, USA

⁵ Department of Physics & Astronomy, University of Leeds, Leeds LS2 9JT, UK

⁶ Computer & Scientific Co. Ltd., 230 Graham Road, Sheffield S10 3GS, UK

⁷ European Space Agency, Vilspa, Apartado 50727, 28080 Madrid, Spain

⁸ School of Physics & Astronomy, University of Birmingham, Edgbaston Birmingham B15 2TT, UK

Received 21 May 2002 / Accepted 27 August 2002

Abstract. We report the results of a multi-wavelength investigation of the O4 V star 9 Sgr (= HD 164794). Our data include observations in the X-ray domain with *XMM-Newton*, in the radio domain with the VLA as well as optical spectroscopy. 9 Sgr is one of a few presumably single OB stars that display non-thermal radio emission. This phenomenon is attributed to synchrotron emission by relativistic electrons accelerated in strong hydrodynamic shocks in the stellar wind. Given the enormous supply of photospheric UV photons in the wind of 9 Sgr, inverse Compton scattering by these relativistic electrons is a priori expected to generate a non-thermal power law tail in the X-ray spectrum. Our EPIC and RGS spectra of 9 Sgr reveal a more complex situation than expected from this simple theoretical picture. While the bulk of the thermal X-ray emission from 9 Sgr arises most probably in a plasma at temperature $\sim 3 \times 10^6$ K distributed throughout the wind, the nature of the hard emission in the X-ray spectrum is less clear. Assuming a non-thermal origin, our best fitting model yields a photon index of ≥ 2.9 for the power law component which would imply a low compression ratio of ≤ 1.79 for the shocks responsible for the electron acceleration. However, the hard emission can also be explained by a thermal plasma at a temperature $\geq 2 \times 10^7$ K. Our VLA data indicate that the radio emission of 9 Sgr was clearly non-thermal at the time of the *XMM-Newton* observation. Again, we derive a low compression ratio (1.7) for the shocks that accelerate the electrons responsible for the synchrotron radio emission. Finally, our optical spectra reveal long-term radial velocity variations suggesting that 9 Sgr could be a long-period spectroscopic binary.

Key words. radiation mechanisms: non-thermal – stars: early-type – stars: individual: 9 Sgr – stars: winds, outflows – X-rays: stars

1. Introduction

X-ray emission from single early-type stars consists mainly of thermal emission from hot plasma at a few million Kelvin located within the stellar wind. Although the origin of the thermal

X-rays is still not fully established, most of the current models focus on shock structures resulting from the line-driven instability as possible loci of the emitting plasma (see Feldmeier et al. 1997 and references therein).

However, the *EINSTEIN*-SSS spectra of three Orion belt stars, revealed X-ray fluxes above 2 keV that were apparently in excess of the thermal flux (Cassinelli & Swank 1983). This led Chen & White (1991, hereafter CW91) to propose that this hard X-ray emission might reflect a non-thermal X-ray component produced through inverse-Compton scattering.

The most prominent indication of non-thermal processes in stellar winds comes from the radio domain (e.g. Bieging et al. 1989). The bulk of the radio emission of luminous OB stars is attributed to thermal free-free radiation produced in the optically thick stellar winds of these objects. However, a subset of OB stars display an often variable non-thermal component on top of their free-free wind emission (see e.g.

Send offprint requests to: G. Rauw,
e-mail: rauw@astro.ulg.ac.be

★ Based on observations with *XMM-Newton*, an ESA Science Mission with instruments and contributions directly funded by ESA Member states and the USA (NASA). Also based on observations collected at the European Southern Observatory (La Silla, Chile) and with the Very Large Array. The VLA is a facility of the National Radio Astronomy Observatory which is operated by the Associated Universities Inc. under cooperative agreement with the National Science Foundation.

★★ Research Associate FNRS (Belgium).

★★★ Research Fellow FNRS (Belgium).

Williams 1996). In wide massive binaries, non-thermal radio emission is likely to arise in the region of stellar wind collision (Eichler & Usov 1993). In the case of single stars, the non-thermal component is believed to result from synchrotron radiation associated with a small population of relativistic electrons accelerated by Fermi processes in shocks located in the outer regions of the stellar wind (e.g. Chen & White 1994). Non-thermal radio emission, if due to synchrotron radiation, is consistent with surface magnetic fields of the order of a hundred Gauss (Chen & White 1994). However, synchrotron radio-emission is expected to account only for a small fraction of the total non-thermal energy budget. In fact, given the enormous supply of photospheric UV photons in the winds of OB stars, inverse-Compton scattering becomes the major energy loss mechanism for relativistic electrons and substantial levels of non-thermal X-ray and low energy γ -rays should be generated, resulting approximately in a power law spectrum from keV to MeV energies (CW91).

The non-thermal X-ray and radio emissions probably arise in distinct regions of the wind. Indeed, the optical depth to hard X-rays throughout the wind is small and inverse-Compton scattering is expected to be most efficient within a few stellar radii where the UV radiation density is highest. On the other hand, as a consequence of the large free-free optical depth at radio frequencies, radio synchrotron emission can only be observed from the outer regions of the wind (beyond about fifty stellar radii). The properties of the non-thermal emission at different energies thus reflect the radial distribution of the relativistic electron spectrum throughout the wind. Detailed models of this distribution rely on stellar parameters, most of which can be well determined from observations in the optical domain. The most noticeable exception in this respect is the stellar magnetic field B_* ¹.

In this context, 9 Sgr (= HD 164794) appeared as a promising target to search for non-thermal X-ray emission. 9 Sgr was considered a probable single O4 V((f)) star by Garmany et al. (1980, but see also Sect. 6). Abbott et al. (1984) discovered non-thermal radio emission with a spectral index² of $\alpha = -0.8$. This non-thermal radio emission varies on ill-determined time scales (Bieging et al. 1989). 9 Sgr has been extensively studied at UV and visible wavelengths and has well determined wind properties. Table 1 lists the parameters adopted in our analysis. Note that the mass loss rate ($\dot{M} = 2.4 \times 10^{-6} M_\odot \text{ yr}^{-1}$) taken from Lamers & Leitherer (1993) was obtained from the H α recombination line rather than from the radio flux which is dominated by the non-thermal emission. Finally, previous X-ray observations of 9 Sgr revealed that this is a relatively bright X-ray source (e.g. Berghöfer et al. 1996).

To search for hard non-thermal X-ray emission in the spectrum of 9 Sgr, we obtained a 20 ksec observation of this target with the *XMM-Newton* observatory. Simultaneously, 9 Sgr

Table 1. Relevant model parameters for 9 Sgr adopted in this paper. The numbers are taken from Conti & Ebbets (1977, CE), Bohannan et al. (1990, BVHA), Lamers & Leitherer (1993, LL) and Shull & van Steenberg (1985, SvS).

Parameter	Ref.
$v_{\text{rot}} \sin i \text{ (km s}^{-1}\text{)}$	128 CE ^a
$T_{\text{eff}} \text{ (K)}$	43 000 BVHA
$R_* (R_\odot)$	16 BVHA
$\log L_{\text{bol}} \text{ (erg s}^{-1}\text{)}$	39.49 BVHA
$d \text{ (kpc)}$	1.58 BVHA
$v_\infty \text{ (km s}^{-1}\text{)}$	2950 LL
$\dot{M} (M_\odot \text{ yr}^{-1})$	2.4×10^{-6} LL
$\log N_{\text{H,ISM}} \text{ (cm}^{-2}\text{)}$	21.34 SvS

^a Note that Penny (1996) derived a somewhat lower $v_{\text{rot}} \sin i$ of 102 km s⁻², but this does not alter any of our conclusions in the following.

was observed at radio wavelengths with the Very Large Array (VLA). A preliminary analysis of the data from this campaign was presented by Rauw et al. (2002). In Sect. 2 of the present paper, we introduce the data from our multi-wavelength campaign including radio, optical and X-ray observations. Sections 3 and 4 deal with the RGS and EPIC spectra of 9 Sgr while the radio and optical data are analysed in Sects. 5 and 6 respectively. Finally, we discuss the overall picture of 9 Sgr that emerges from our campaign and present our conclusions in Sect. 7.

2. Observations

2.1. X-ray data

9 Sgr was observed with *XMM-Newton* (Jansen et al. 2001) during revolution 228 on March 8, 2001 (JD 2451976.978–2451977.239). The two EPIC MOS instruments were operated in the full frame mode (Turner et al. 2001) whilst the EPIC-pn camera was used in the extended full frame mode (Strüder et al. 2001). All three EPIC instruments used the thick filter to reject optical light. The two RGS instruments were operated in the default spectroscopy mode (den Herder et al. 2001).

We used version 5.1 of the *XMM-Newton* Science Analysis System (SAS) to reduce the raw EPIC data. For the MOS (resp. pn) observations only events with pattern 0–12 (resp. 0) were considered (Turner et al. 2001). No indication of pile-up was apparent in the data.

The RGS observations were processed with version 5.0.1 of the SAS. Appropriate response matrices were generated using the “rgsrmfgen” SAS task.

The EPIC data are significantly affected by straylight photons from the LMXB GX 9+1 (= Sgr X-3) located at 1° from the center of the FOV. For the pn detector the straylight features appear as arcs that are not exactly concentric due to the slight imperfections of the mirror module alignment. On the MOS images the arcs are truncated because of the Reflection Grating Assemblies (RGAs) which are mounted on the mirror modules associated with the MOS instruments. In addition, the

¹ So far, magnetic fields have only been detected for a few early-type OB stars (~ 360 G in β Cep and ~ 1100 G in θ^1 Ori C see Donati et al. 2001, 2002). For most OB stars, the non-detection of the Zeeman effect puts an upper limit of order ~ 100 G on B_* (Mathys 1999).

² The radio spectral index α is defined by $F_\nu \propto \nu^\alpha$. Purely thermal sources have $\alpha \approx 0.6$ (Wright & Barlow 1975).

Table 2. Effective exposure times and background corrected count rates of 9 Sgr as measured with the instruments onboard *XMM* (see the text for details on the source and background extraction). The count rates for the EPIC instruments are given in the energy range 0.2–10 keV.

	MOS1	MOS2	pn	RGS1	RGS2
Exp. (s)	21 880	21 881	17 474	23 100	23 100
Rate (cts s ⁻¹)	0.269 ± 0.004	0.280 ± 0.004	0.819 ± 0.007	$(3.61 \pm 0.39) \times 10^{-2}$	$(5.16 \pm 0.51) \times 10^{-2}$

straylight arcs in the MOS images display some extended tails. The intensity of these tails decreases with increasing angular distance from GX 9+1 (see Fig. 1).

The straylight is produced by photons that are singly reflected by the mirror hyperbolas. Although the straylight collecting area is only a few square centimeters (Stockman et al. 1998), the brightness of GX 9+1 compared to the sources in our field of view leads to a serious contamination of our data. The straylight photons are rather hard. In fact, images extracted in the soft energy range $PI \in]200, 1500[$ ($\sim E \in]0.2, 1.5[$ keV) reveal a negligible contamination level (see Fig. 2).

Because of the complex reflection pattern, one can expect the spectrum of the straylight features to be distorted compared to the actual spectrum of GX 9+1. Schulz (1999) fitted the ROSAT spectrum of GX 9+1 using a blackbody model with $N_H = 1.36 \times 10^{22} \text{ cm}^{-2}$ and $kT = 0.98 \pm 0.06 \text{ keV}$. The spectrum of the brightest straylight arc in the MOS1 detector is shown in the left panel of Fig. 2. Generally speaking, the best fitting spectral parameters depend slightly on the instrument and on the location of the straylight feature considered. In all the cases the straylight spectrum is best fitted by a heavily absorbed blackbody model with N_H in the range 2.05×10^{22} (MOS2) – $3.46 \times 10^{22} \text{ cm}^{-2}$ (pn) and with a temperature kT between 0.99 (pn) and 1.21 keV (MOS2).

2.2. Radio data

We observed 9 Sgr with the NRAO Very Large Array (VLA) simultaneously (JD 2451977.012–037) with the *XMM-Newton* observations. Data were collected at 3.6 cm (*X*-band), 6 cm (*C*-band) and 20 cm (*L*-band). At each wavelength, we observed the flux calibrator 3C 286 = 1331+305 (J2000). The observation on 9 Sgr took 8 min for each wavelength, and was preceded and followed by an observation of the phase calibrator 1751-253 (J2000). All observations were made in two sidebands (denoted IF1 and IF2), each of which has a bandwidth of 50 MHz. The VLA was in the B configuration, with the antenna at position N 32 missing.

The data reduction was done using the Astronomical Image Processing System (AIPS, version 31DEC01), developed by the NRAO. From the observed visibilities of the calibrators, the instrumental gains are determined and discrepant points flagged. The gains are interpolated in time and applied to the 9 Sgr visibilities. Applying the Fourier transform to these calibrated visibilities turns them into an intensity map (called the dirty map). The weighting scheme used is robust uniform (Briggs 1995). The images are then deconvolved to remove the effect of the beam, using the CLEAN algorithm as implemented in AIPS (Cornwell & Braun 1989). In the reduction procedure we ap-

plied the available baseline corrections. The fluxes assigned to the flux calibrator are given in Table 3.

Table 3. Fluxes of the flux calibrator 3C 286. The fluxes are based on the 1995.2 VLA coefficients (Perley & Taylor 1999). The two values for each entry correspond to the two 50 MHz sidebands (IF1 and IF2).

λ (cm)	Frequency (GHz)	Flux (Jy)
3.6	8.4351	5.2158
	8.4851	5.1947
6	4.8351	7.5100
	4.8851	7.4620
20	1.3851	14.9031
	1.4649	14.5108

The major problem in the reduction of our VLA data is the presence of other, high-intensity, sources in the field. First of all, 9 Sgr is just in front of the Lagoon Nebula (M 8), which appears as a spatially extended source with a high radio flux. Due to the filtering properties of a radio-interferometer, a large part of this flux will not be seen by the instrument. While observations made in the VLA A-configuration show almost no residual background from M 8, our observations (made in the B-configuration) do show some M 8 flux. As the spatial resolution decreases with wavelength, this effect is worst at 20 cm. Secondly, there are strong compact sources in the field (associated with the Hourglass H II region). The sidelobes of these sources can be seen on the dirty map to extend beyond the position of 9 Sgr. At 20 cm, sidelobes from TXS 1801-245 are also important.

To eliminate the effect of the M 8 nebula, we dropped all observational data taken on the shortest baselines (using the keyword `uvrange` in the AIPS task “`imagr`”). To eliminate the sidelobes of the Hourglass and TXS 1801-245 we made sure that these sources were included in the field on which the cleaning algorithm was applied.

2.3. Optical data

A set of echelle spectra of 9 Sgr was gathered with the Fiber-fed Extended Range Optical Spectrograph (FEROS, Kaufer et al. 1999) attached to the ESO 1.52 m telescope at La Silla, during two observing runs in May 2000 and 2001. Typical exposure times were of the order of five minutes. The spectral resolving power of the FEROS instrument is 48 000. The detector was an EEV CCD with 2048×4096 pixels of $15 \mu\text{m} \times 15 \mu\text{m}$. For a detailed description of the spectrograph, we refer to the paper of Kaufer et al. (1999). We used a slightly modified version of the FEROS context within the MIDAS package provided by ESO to reduce the data.

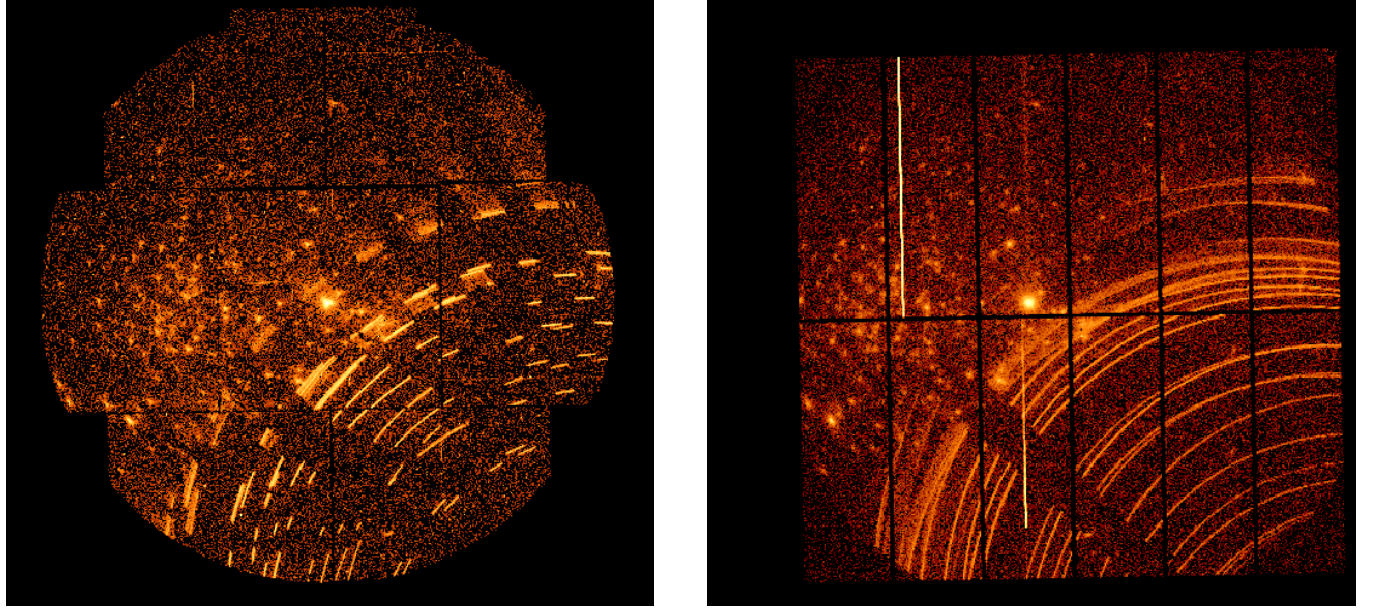


Fig. 1. EPIC MOS2 (left panel) and EPIC-pn (right panel) broad-band images around 9 Sgr. The images are displayed with a logarithmic scale.

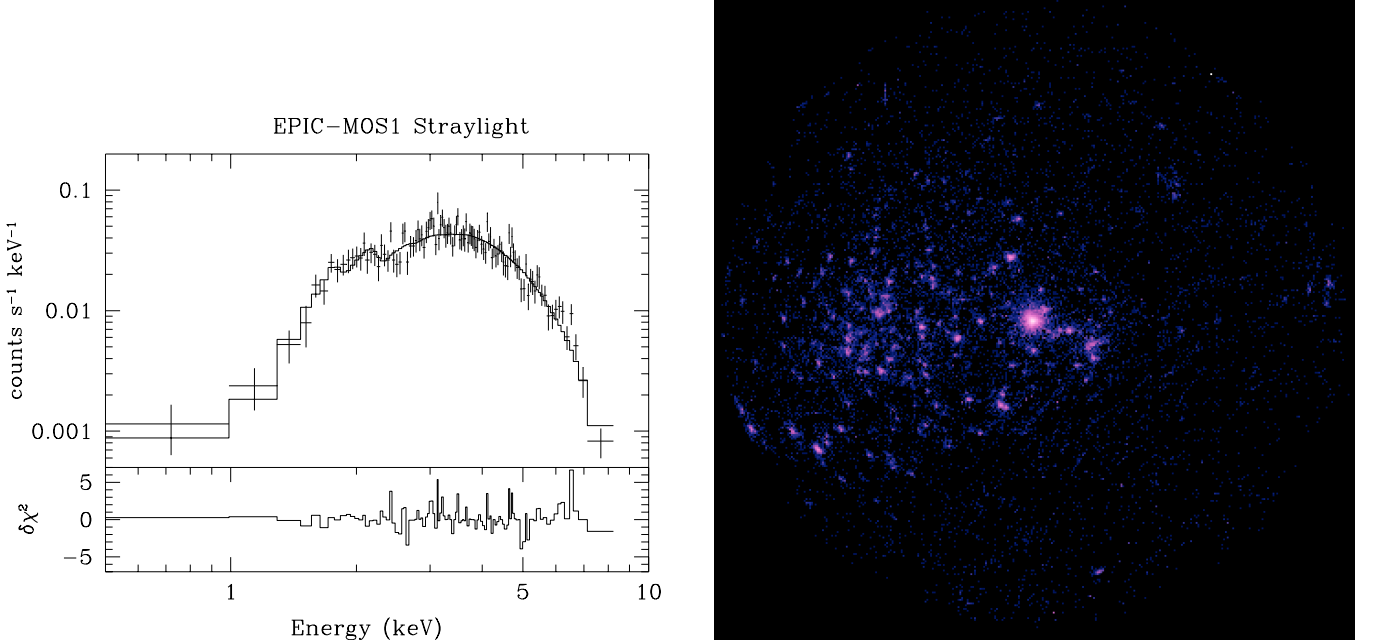


Fig. 2. Left panel: spectrum of the brightest straylight feature in the EPIC-MOS1 image. The energy distribution can be fitted with a heavily absorbed ($N_{\text{H}} = (3.1 \pm 0.3) \times 10^{22} \text{ cm}^{-2}$) blackbody model of temperature $kT = 1.04 \pm 0.05 \text{ keV}$. Right panel: combined EPIC MOS1 + MOS2 image extracted over the PI range from 200 to 1500. The image is displayed with a logarithmic scale. The faint sources near 9 Sgr are associated with the young open cluster NGC 6530 inside the Lagoon Nebula. These sources are discussed in a separate paper.

3. The RGS spectrum of 9 Sgr

At first glance, the RGS spectrum of 9 Sgr is reminiscent of that of the O4 Ief star ζ Pup (Kahn et al. 2001) and of the *Chandra*-HETG spectrum of ζ Ori (O9.7 Ib, Waldron & Cassinelli 2001). We observe the He-like triplets of Ne IX and O VII, the Ly α lines of Ne X, O VIII and N VII as well as several L-shell lines of Fe XVII. One difference between ζ Pup and 9 Sgr concerns the relative strength of the nitrogen and oxygen lines: while in ζ Pup, the N/O ratio is enhanced with respect to solar abundances, we find no indication of such an effect in 9 Sgr.

Given the limited *S/N* of our RGS spectra, little can be said about the detailed morphology of the emission lines. However, we fitted the emission line profiles with Gaussians to determine the line fluxes and centroids (Table 4). The continuum strength was determined from fluxes on each side of the line. We caution that unresolved blends of weak emission lines could mimic a pseudo-continuum that would affect the net line intensities. In this case, our fitted line intensities should provide lower limits to the actual line fluxes.

Table 4. Fluxes and centroid shifts of the most prominent emission lines in the spectrum of 9 Sgr.

	Flux (photons $\text{cm}^{-2} \text{s}^{-1}$)	Velocity shift (km s^{-1})
Ne X $\lambda 12.13$	$(3.5 \pm 1.6) \times 10^{-5}$	-660 ± 290
Fe XVII $\lambda\lambda 16.78-17.10$	$(8.1 \pm 2.0) \times 10^{-5}$	-730 ± 280
O VIII $\lambda 18.97$	$(8.2 \pm 1.5) \times 10^{-5}$	-540 ± 230
N VII $\lambda 24.78$	$(4.1 \pm 1.7) \times 10^{-5}$	-60 ± 600

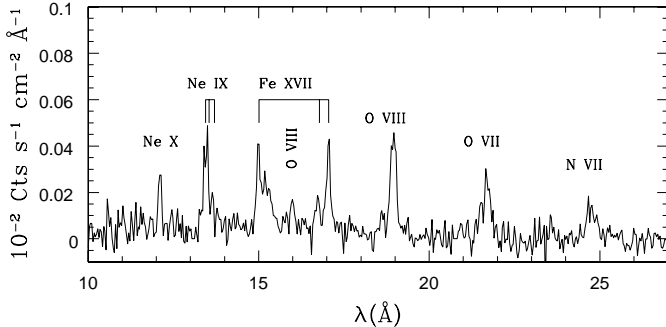


Fig. 3. Combined RGS1+2 first order spectrum of 9 Sgr.

The lines are broad with half widths at half maximum in the range $500-1600 \text{ km s}^{-1}$. Our data reveal a slight blue-shift of the line centroids in all strong lines. The blue-shift is expected for lines formed in an accelerating stellar wind since radiation from the approaching side of the wind should be less attenuated by continuum opacity than that from the receding part (Owocki & Cohen 2001).

Grating spectra obtained with *XMM-Newton* and *Chandra* have provided new insight into the X-ray properties of hot early-type stars. For instance, the He-like resonance (r), intercombination (i) and forbidden (f) lines have been used to infer the location of the X-ray emitting material within the stellar wind (see e.g. Waldron & Cassinelli 2001). In the presence of a strong ultraviolet radiation field, as in the atmospheres of early-type stars, the transition $2^3\text{S} \rightarrow 2^3\text{P}$ is essentially excited by the UV radiation. Hence the ratio $\mathcal{R} = f/i$ is no longer determined by the density of the plasma but rather by the intensity of the UV radiation (e.g. Porquet et al. 2001).

In the case of 9 Sgr, the f component is clearly detected in the Ne IX triplet whilst it is not detected for O VII (Table 5). The non-detection of the O VII f line leaves us with an upper limit of 0.2 on the corresponding \mathcal{R} ratio.

We compared the observed \mathcal{R} ratio of Ne IX with the theoretical values of Porquet et al. (2001) corresponding to radiation temperatures³ of 30 000 and 40 000 K and an electron temperature of $3 \times 10^6 \text{ K}$ (consistent with the temperature inferred from our EPIC spectra of 9 Sgr, Tables 6–8). This comparison suggests that the Ne IX line forms at rather low values of the

Table 5. Line intensity ratios of the He-like *fir* triplets in the RGS spectra of 9 Sgr. The error bars correspond to the 90% confidence ranges as determined from our fits.

	Ne IX	O VII
f/i	0.31 ± 0.27	<0.2
r/i	0.74 ± 0.43	0.37 ± 0.33

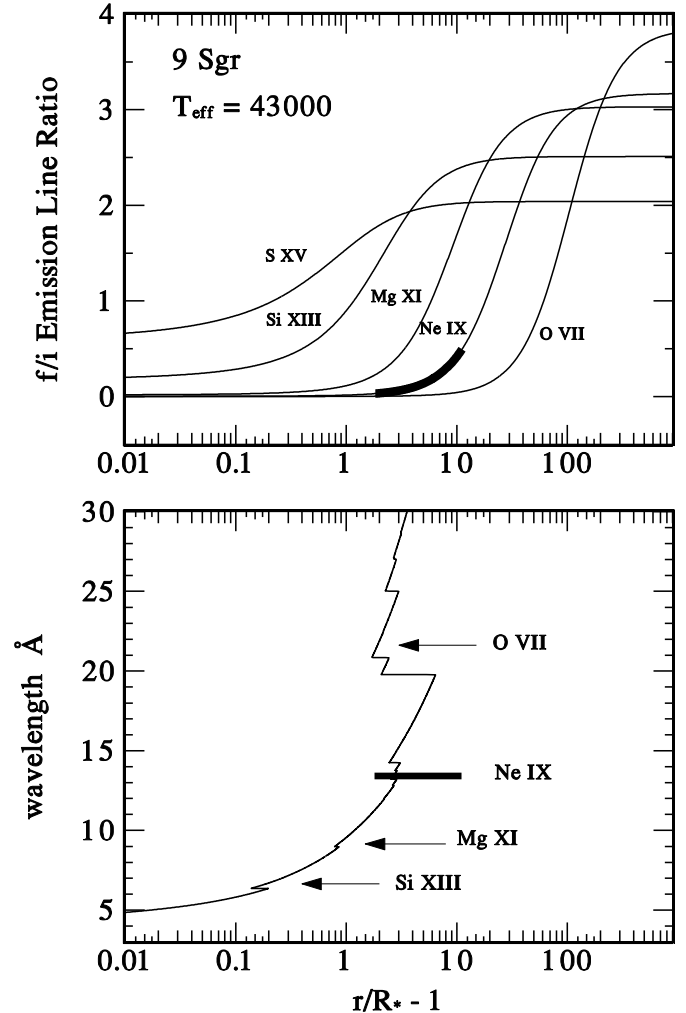


Fig. 4. Upper panel: predicted dependence of the $\mathcal{R} = f/i$ ratio for helium-like triplets of various ions in the stellar wind of 9 Sgr. The heavy solid line indicates the 90% confidence range on \mathcal{R} for the Ne IX triplet. Lower panel: radius of radial optical depth unity as a function of wavelength. The wavelengths of various helium-like triplets are indicated and the probable location of the Ne IX line formation region (corresponding to the uncertainty range on the \mathcal{R} ratio) is indicated by the heavy line.

dilution factor $w = 0.5(1 - \sqrt{1 - R_*/r}) \sim 0.01$ and thus far out in the wind (probably beyond several R_*).

We used the formalism outlined by Waldron & Cassinelli (2001) to further constrain the location of the line emitting plasma. The predicted radial dependence of the \mathcal{R} ratios for various ions in the wind of 9 Sgr was computed including the effects of collisions and radiative transitions, accounting for the photospheric UV flux at $T_{\text{eff}} = 43 000 \text{ K}$. The results are shown in Fig. 4. The observed 90% confidence range of \mathcal{R} for the Ne IX

³ Torres (1987) showed that the UV energy distribution of 9 Sgr can be matched with model atmospheres corresponding to temperatures of 35 000 and 40 000 K. A radiation temperature of 30 000 K thus probably yields a lower limit to the actual temperature.

triplet is displayed by the heavy line. The results of our analysis suggest that the Ne IX line forms somewhere between 3 and $11 R_*$.

At radii below $\sim 50 R_*$, the \mathcal{R} ratio of O VII varies very slowly as a function of radius (Fig. 4). Hence, the upper limit of $\mathcal{R} < 0.2$ is consistent with the oxygen triad forming anywhere between the stellar surface and about $25 R_*$.

A word of caution is necessary though: in addition to the Ne IX triplet, the spectral range 13.3 to 13.8 Å harbors a huge number of iron lines from various ionization stages: Fe XVIII – XXI. Most of these lines have maximum emissivities that are more than a factor ten lower than those of the Ne IX lines (see e.g. the line list of the SPEX plasma code at <http://www.sron.nl/divisions/hea/index.html>, Kaastra et al. 2002). Although the EPIC spectra suggest a multi-temperature plasma that could give rise to a rather broad range of ionization stages, the RGS data only reveal strong iron lines corresponding to Fe XVII. Blends with lines from Fe XX and Fe XXI probably do not have a significant impact on the neon triplet since other iron lines of these species that are expected to be strong are either absent or only marginally detected. The strongest contamination could arise from the Fe XIX lines at 13.51 and 13.52 Å that are blended with the Ne IX intercombination line and have maximum emissivities exceeding that of the i line. Conversely, the 13.73–13.74 Å lines of the Fe XIX ion affect the Ne IX f line but these lines have maximum emissivities that are about a factor ten lower than those of the lines at 13.51 and 13.52 Å. In any case, the lack of a significant Fe XIX emission at 14.67 and 16.11 Å suggests that the effect of this ion on the Ne IX \mathcal{R} ratio should be pretty low.

The bottom panel of Fig. 4 displays the radius of continuum optical depth unity in the stellar wind of 9 Sgr as a function of wavelength. The circumstellar opacity was computed using the wind absorption model of Waldron et al. (1998) adopting the parameters from Table 1 and assuming a homogeneous and spherically symmetric wind. As can be seen from this figure, the bulk of the Ne line emission arises from outside the radius of radial optical depth unity. This result is quite similar to the situation for other O-stars (see e.g. in ζ Pup, Kahn et al. 2001; Cassinelli et al. 2001; ζ Ori, Waldron & Cassinelli 2001).

Let us briefly return to the blue-shift of the lines seen in Table 4. Within the large error bars, it is hard to uncover any trend (e.g. between the velocity shift and the ionization potential of the specific ions): all velocity shifts are roughly consistent with the same value. Our results from the *fir* analysis above suggest that the bulk of the line emission will have to come from radii beyond $\tau = 1$ (though not too far outwards because of the dependence of the line emission measure on the square of the density). From Fig. 4, it appears that $\tau = 1$ occurs between ~ 3 and $7 R_*$ for the four lines listed in Table 4. However, there appears no correlation between the velocity shift and $R(\tau = 1)$ neither. For instance, the N VII and Ne X lines correspond roughly to the same $R(\tau = 1) \in [3, 4] R_*$ but have different velocity shifts, although their error bars do overlap.

4. The EPIC spectrum of 9 Sgr

The contamination of the EPIC data by the straylight considerably complicates the extraction of the spectrum of 9 Sgr and of the background. The worst situation is probably encountered for the MOS1 camera.

For all three EPIC cameras, the source spectrum was accumulated over a radius of $45''$ excluding the intersection with a small circular region centered on a faint point-like source at RA = 18 : 03 : 50 and DEC = –24 : 21 : 10 (Equinox 2000.0). For the pn detector, the extraction region was further truncated to avoid the gap between the CCDs. Let us recall that the straylight is essentially concentrated in the arcs except for the extended tails in the MOS images described in Sect. 2.1. Figure 5 reveals that the source spectrum of 9 Sgr should be free from any contamination at least in the MOS2 and pn data. However, a low level contamination of the MOS1 source spectrum of 9 Sgr cannot be fully excluded.

The background spectra for the different data sets were obtained over rectangular areas trying to avoid the straylight features (see Fig. 5). We have also tested a different background subtraction technique using the blank sky event lists provided by the *XMM-SOC*. The resulting background subtracted spectra of 9 Sgr do not show any significant differences compared to those obtained with the technique described hereabove.

We adopted the redistribution matrices (rmfs) provided by the EPIC instrument teams (versions available in May 2001) and we used the sas to build the appropriate ancillary response file (arf) for each EPIC instrument. The spectra were binned to reach a minimum of 10 counts per channel and the background corrected spectra were analyzed using the XSPEC software (version 11.00). Because of the strong noise in the pn detector below 0.2 keV and the calibration uncertainties of the EPIC instruments at low energies, we ignored the binned energy channels below 0.2 keV for the XSPEC fits.

4.1. Fitting simple models

We tested a couple of rather simple models. In these fits, we always fixed the interstellar H I column density at $0.22 \times 10^{22} \text{ cm}^{-2}$. The latter value was adopted from the work of Shull & van Steenberg (1985). These authors evaluated the neutral hydrogen column density towards 9 Sgr using high-resolution *IUE* observations of the interstellar Ly α line. Their result, $N_{\text{H,ISM}} = (0.22 \pm 0.03) \times 10^{22} \text{ cm}^{-2}$, is in fair agreement with the observed $E(B - V)$ colour excess of 9 Sgr assuming a “normal” gas to dust ratio and the results of a similar study by Diplas & Savage (1994) who determined $N_{\text{H,ISM}} = (0.19^{+0.04}_{-0.02}) \times 10^{22} \text{ cm}^{-2}$. As a first approximation, we modelled the circumstellar (i.e. wind) absorption using neutral ISM opacities⁴.

The background-corrected EPIC spectra of 9 Sgr display a break around ~ 2.5 keV with extra emission above it. Absorbed single-temperature mekal models for optically thin plasmas (Mewe et al. 1985; Kaastra 1992) hence do not provide

⁴ This is a crude approximation. Below we use a proper model to simulate the wind absorption.

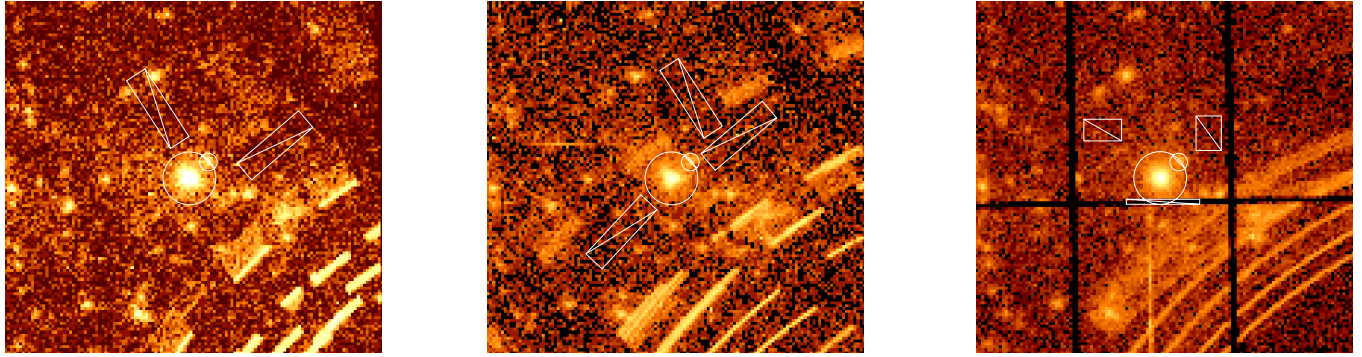


Fig. 5. Zoom on the source and background regions for the three EPIC instruments. From left to right, the images correspond to the MOS1, MOS2 and pn data. Note that the images are displayed with a logarithmic scale. The small circular region around the faint point source to the NW of 9 Sgr was excluded from the source region.

acceptable fits for any of the instruments. Two temperature **mekal** models still yield a reduced $\chi^2_\nu > 2$ except for the pn spectrum ($\chi^2_\nu = 1.49$). The best fit temperatures are about 0.23 and ~ 0.6 keV for all three instruments. It should be noted that the best-fit column density of the softest **mekal** component is always zero. This is most probably a consequence of the poor representation of the wind absorption by the neutral ISM opacities.

The quality of the fits improves for 1-T **mekal** + power law models (χ^2_ν between 1.31 and 1.79). However, these fits systematically yield photon indices ($\Gamma \geq 3.8$) much larger than the value (~ 1.5) expected from the Chen & White (1991) model. One reason for this steep power law could be that the thermal plasma model underestimates the observed flux at energies below 0.5 keV and the power law has to provide some flux to compensate this. One should also note that the column density of the power law component is again very close to or equal to zero.

Note that requiring a value of $\Gamma = 1.5$ in the 1-T **mekal** + power law models yields an unacceptably large $\chi^2_\nu \simeq 2$ for all EPIC spectra. We have also tested 2-T **mekal** + power law models. Again requiring $\Gamma = 1.5$, we obtain $\chi^2_\nu = 1.64$ for a simultaneous fit of the EPIC + RGS data set with two temperatures of 0.22 and 0.59 keV. Allowing the photon index to deviate from 1.5, a better fit ($\chi^2_\nu = 1.34$) is achieved for $\Gamma = 3.9$, $kT_1 = 0.18$ and $kT_2 = 0.51$ keV.

To simulate a possible contamination of the EPIC spectra of 9 Sgr by the straylight, we have also tested models where we included an absorbed blackbody with a column density between 2.0 and 3.5×10^{22} cm $^{-2}$ and a temperature in the range 0.99–1.21 keV. Including a straylight component in the fits does not improve their quality and does not alter the best fitting parameters of the **mekal** and/or power law components.

Including the RGS spectra in the fits allows to better constrain the lower energy components of the model. However, since our RGS data do not reveal any feature longwards of ~ 27 Å (either because of the interstellar + circumstellar absorption or because of the intrinsic lack of lines in the source spectrum at these wavelengths), they cannot help constrain the contribution of the power law component to the flux at low energies ($E < 0.5$ keV).

Since there could be some uncertainties on the EPIC calibration at lower energies, we have also repeated the spectral fitting ignoring all the energy channels below 0.5 keV. The best fitting **mekal** + power law model turns out to be rather insensitive to these energy channels and we recover the same parameters as above.

Finally, we have also fitted 1-T **mekal** + broken power law models. For the broken power law models, we adopted

$$\begin{aligned} \eta &= \eta(E_0) && \text{for } E \leq E_0 \\ \eta &= \eta(E_0)(E/E_0)^{-\Gamma+1} && \text{for } E > E_0 \end{aligned}$$

where η stands for the spectral emissivity and Γ corresponds to the photon index of the power law above the low energy cut-off E_0 . Due to various cooling processes and the interaction with thermal electrons, one expects the energy spectrum of relativistic electrons in stellar winds to possess a low energy cut-off. CW91 argue that for O-star winds, this cut-off should translate into an inverse Compton low energy cut-off of order 0.2 keV. However, the exact value depends on a number of stellar parameters and we can therefore not rule out the existence of a low energy cut-off in the inverse Compton power law spectrum within the energy range covered by our EPIC spectra.

We fitted the EPIC data setting E_0 to 0.5, 1.0 or 2.0 keV. By requiring a flat spectrum below E_0 , we strongly limit the contribution of the non-thermal component to the flux at low energies. For $E_0 = 0.5$ keV, we obtain a good fit ($\chi^2_\nu = 1.26$ for the pn data set) with $\Gamma \simeq 4.0$ while the parameters of the thermal component remain unchanged. For increasing values of E_0 , the value of Γ increases while the quality of the fit decreases.

4.2. Using a wind absorption model

To solve the problems due to the poor modelling of the circumstellar opacity, we have used a wind absorption model (Waldron et al. 1998) computed with the parameters from Table 1. The EPIC spectra of 9 Sgr are fitted with models accounting for the absorption by the ionized wind in addition to the neutral ISM material (the latter corresponds to a fixed column density of 0.22×10^{22} cm $^{-2}$). The fits are obtained by varying the temperature (or power law index), the wind column density and the emission measure.

We started by testing 2-T `mekal` models including the effects of wind opacity. The results are listed in Table 6 below. The inclusion of the wind absorption cross section significantly improves the quality of the fits at energies below 0.5 keV. However, above 2 keV the model still underestimates the observed energy distribution.

We subsequently fitted the EPIC-pn spectrum of 9 Sgr with a 1-T `mekal` + broken power law model. The results are listed in Table 7. We note that the overall quality of the fits is quite comparable to that of the 2-T fits. However, while the power law models fit the high energy tail, the 2-T models yield a better fit to the Si XIII lines at ~ 1.86 keV. Again, we note that Γ depends on the value of the low energy cut-off. However, the values of $\Gamma \geq 2.9$ obtained here are lower than those obtained with the models that assume a neutral absorption column. The inclusion of a proper wind absorption column allows to fit the low energy part of the spectrum by the sole contribution of the thermal component, while this was not the case for the models in Sect. 4.1. Therefore in the current fits, the power law component is far less sensitive to the low energy part of the spectrum than in the fits of Sect. 4.1.

Finally, we note that the EPIC-pn spectrum suggests the presence of an Fe K α line, although this feature is not seen in the MOS spectra and its existence needs thus to be confirmed by other observations. The possible presence of an Fe K α line suggests that the hard X-ray continuum could be thermal. These considerations prompted us to fit the EPIC spectra of 9 Sgr with 3-T thermal models. The derived best fit parameters are roughly equal for all three instruments. The third, high temperature, component is however not well constrained. In Fig. 6, we used $kT_3 = 8.6$ keV and $N_{\text{wind},3} = 4.5 \times 10^{22} \text{ cm}^{-2}$ (corresponding to the maximum wind column density for 9 Sgr). These values provide the best fit, but from a statistical point of view, the fit is not much different from that corresponding to the lower limit values of Table 8.

In summary, we find that, provided the wind absorption is properly treated, the EPIC spectra of 9 Sgr can be fitted equally well either by a multi-temperature thermal model including plasma at a temperature exceeding $\sim 2 \times 10^7$ K, or by a model including a non-thermal power law component with a photon index $\Gamma \geq 2.9$.

5. Simultaneous VLA radio observations

We used the AIPS task “`jmf`” to measure the flux on the cleaned radio maps by fitting an elliptical Gaussian to the source. The Gaussian has the same shape as the cleaned beam, so the position and total flux are the only parameters fitted. A comparison between the peak intensity and the flux resulting from the fit shows that 9 Sgr is indeed a point source. Each flux determination is given an error bar equal to the rms in the field.

However, the major source of error in the fluxes is not the statistical noise in the map, but rather the uncertainty in the background subtraction. Various combinations of `uvrange` and depth of cleaning (see Sect. 2.2) give cleaned maps that are acceptably smooth, showing that all background and sidelobe effects have been removed (see Fig. 7). Rather than using a single combination of `uvrange` and depth of cleaning to determine

the flux, we opted to look at the whole range spanned by all acceptable combinations. In doing so we did not clean deeper than was necessary for a given `uvrange` (cleaning too deep can easily lower the flux by 1σ). The resulting fluxes (see Table 9) are then determined by taking the average of the highest and the lowest value of the range. We added to the highest value its rms, and we subtracted from the lowest value its rms. The resulting error bar is given by the range between the average and lowest/highest value. The error bars are sufficiently large that we consider them to include the 1–5% calibration error.

To judge the robustness of our flux determination, we repeated the reduction, tapering the weights of longer baselines, or using natural weighting instead of robust uniform weighting. As almost all results fall within the error bar, we conclude that the error bars we derived correctly reflect the accuracy of the result.

The spectral indices (α) are given in Table 9, as well as the error bars which were derived from the theory of propagation of errors. For a thermal spectrum due to free-free radiation in the wind, one expects $\alpha \simeq +0.6$ (e.g. Wright & Barlow 1975). The 9 Sgr spectral indices are negative, clearly indicating the non-thermal character of the radio emission.

The radio flux of 9 Sgr is known to be variable (Bieging et al. 1989). Our 6 cm flux is high compared to previous values, but the error bar still overlaps the range covered by values in the literature (see Table 9). Our value for 20 cm seems higher than the Bieging et al. ones (3.6–3.9 mJy): however, when we reduce their dataset, we tend to derive higher fluxes than they did. As far as we know, no 3.6 cm fluxes have been published. We did have a look at some of the 3.6 cm observations in the VLA archive. The present observation falls within the range of the archive data, but is again in the very upper part of that range.

5.1. A simple model

In this section we attempt to fit the VLA observations of 9 Sgr with a simple theoretical model. As pointed out in the introduction, the non-thermal radio emission is believed to be synchrotron radiation from relativistic electrons (White 1985). In the presence of shocks and of a magnetic field, electrons are accelerated to high energies (Bell 1978) through the first-order Fermi mechanism (Fermi 1949), resulting in a power law distribution for the momentum p of the accelerated particles. The radio flux originating from a distribution $N(p, r)$ of relativistic electrons, can be expressed as

$$F_\nu = \frac{1}{4\pi D^2} \int_{R_\nu}^{R_{\max}} dr 4\pi r^2 \int_{p_0}^{\infty} dp N(p, r) P_\nu(B(r), p) \quad (1)$$

where P_ν is the emissivity for a single relativistic electron (Rybicki & Lightman 1979), integrated over solid angle, $B(r)$ the magnetic field at radius r and D the distance to the star. For the lower momentum cut-off of the power law, we took $p_0 = 1 \text{ MeV}/c$ (CW91). $B(r)$ is related to the surface field B_* through

$$B(r) = B_* \frac{v_{\text{rot}}}{v_\infty} \frac{R_*}{r}. \quad (2)$$

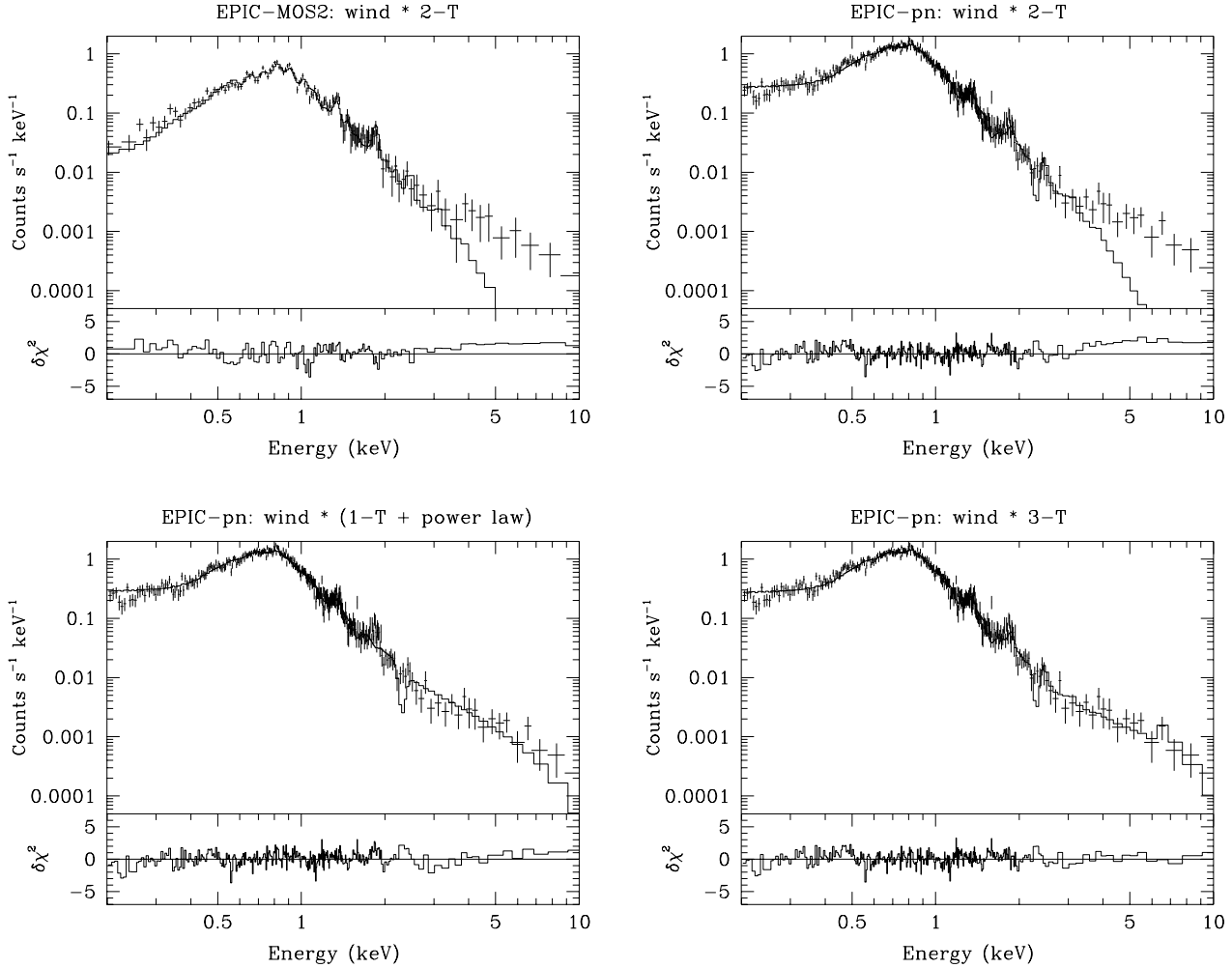


Fig. 6. The EPIC spectrum of 9 Sgr together with different best-fitting models. The different panels illustrate the best fitting 2-T thermal model with realistic wind absorption cross sections for the MOS2 (upper left panel) and the pn (upper right panel), the 1-T + broken power law model together with a wind absorption model (lower left panel) and the 3-T thermal model with wind absorption (lower right panel).

Table 6. Best fitting parameters of the 2-T thermal model fits with a wind opacity model ($w_{\text{abs,ISM}} * (w_{\text{abs,wind,1}} * \text{mekal}_1 + w_{\text{abs,wind,2}} * \text{mekal}_2)$). A fixed interstellar column density of $0.22 \times 10^{22} \text{ cm}^{-2}$ has been applied to the model. The metallicity was fixed at solar. EM is the emission measure defined by $EM = \int_V n_e n_H \text{ d}V$ where n_e and n_H stand respectively for the electron and proton density in the X-ray emitting plasma. The observed spectral flux measured at Earth at energy E is then given by $f(E) = \frac{1}{4\pi D^2} \eta(E, T) EM$, where $\eta(E, T)$ stands for the emissivity as a function of temperature and energy. f_X yields the observed (i.e. absorbed) flux integrated over the energy band 0.2–10.0 keV (in units $10^{-12} \text{ erg cm}^{-2} \text{ s}^{-1}$). The number of degrees of freedom is provided between brackets in Col. 8.

Inst.	$N_{\text{wind,1}}$ (10^{22} cm^{-2})	kT_1 (keV)	$\log EM_1$ (cm^{-3})	$N_{\text{wind,2}}$ (10^{22} cm^{-2})	kT_2 (keV)	$\log EM_2$ (cm^{-3})	χ^2_ν	f_X
MOS1	0.34 ± 0.16	0.26 ± 0.01	56.22	1.10 ± 0.71	0.78 ± 0.17	55.47	1.86 (122)	1.64
MOS2	0.29 ± 0.14	0.25 ± 0.01	56.19	0.97 ± 0.63	0.71 ± 0.15	55.56	1.44 (124)	1.71
pn	0.28 ± 0.09	0.26 ± 0.01	56.20	1.64 ± 0.62	0.69 ± 0.27	55.79	1.19 (316)	1.84

Table 7. Same as Table 6, but for the best fitting parameters of 1-T mekal + broken power law fits to the EPIC-pn spectrum of 9 Sgr. Γ stands for the photon index of the power law above the low energy cut-off E_0 (below E_0 the photon index is equal to 1), while K yields the normalization factor of the broken power law (in photons $\text{s}^{-1} \text{ cm}^{-2} \text{ keV}^{-1}$ at 1 keV).

E_0 (keV)	$N_{\text{H,1}}$ (10^{22} cm^{-2})	kT (keV)	$\log EM$ (cm^{-3})	$N_{\text{H,2}}$ (10^{22} cm^{-2})	Γ	K	χ^2_ν	f_X
0.5	0.28 ± 0.09	0.26 ± 0.01	56.16	<0.9	2.92 ± 0.59	7.11×10^{-4}	1.14 (316)	1.84
1.0	0.28 ± 0.09	0.26 ± 0.01	56.19	<1.3	3.40 ± 0.80	8.17×10^{-4}	1.14 (316)	1.83
2.0	0.28 ± 0.09	0.26 ± 0.01	56.20	<2.0	4.33 ± 2.18	2.18×10^{-4}	1.26 (316)	1.81

Table 8. Best fitting parameters of 3-T thermal model fit with a wind opacity model ($w_{\text{abs,ISM}}^*$ ($w_{\text{abs,wind,1}}^* \text{mekal}_1 + w_{\text{abs,wind,2}}^* \text{mekal}_2 + w_{\text{abs,wind,3}}^* \text{mekal}_3$)). A fixed interstellar column density of $0.22 \times 10^{22} \text{ cm}^{-2}$ has been applied to the model. The metallicity was fixed at solar.

Inst.	$N_{\text{wind,1}}$ (10^{22} cm^{-2})	kT_1 (keV)	$\log EM_1$ (cm^{-3})	$N_{\text{wind,2}}$ (10^{22} cm^{-2})	kT_2 (keV)	$\log EM_2$ (cm^{-3})	$N_{\text{wind,3}}$ (10^{22} cm^{-2})	kT_3 (keV)	$\log EM_3$ (cm^{-3})	χ^2_v
M1	0.34 ± 0.16	0.26 ± 0.01	56.22	1.06 ± 0.68	0.71 ± 0.15	55.48	>0.63	>1.46	54.71	1.70 (118)
M2	0.29 ± 0.14	0.25 ± 0.01	56.23	0.86 ± 0.56	0.73 ± 0.16	55.52	>0.63	>1.46	54.71	1.33 (120)
pn	0.28 ± 0.09	0.26 ± 0.01	56.22	1.65 ± 0.62	0.67 ± 0.26	55.83	>0.63	>1.46	54.68	1.08 (312)

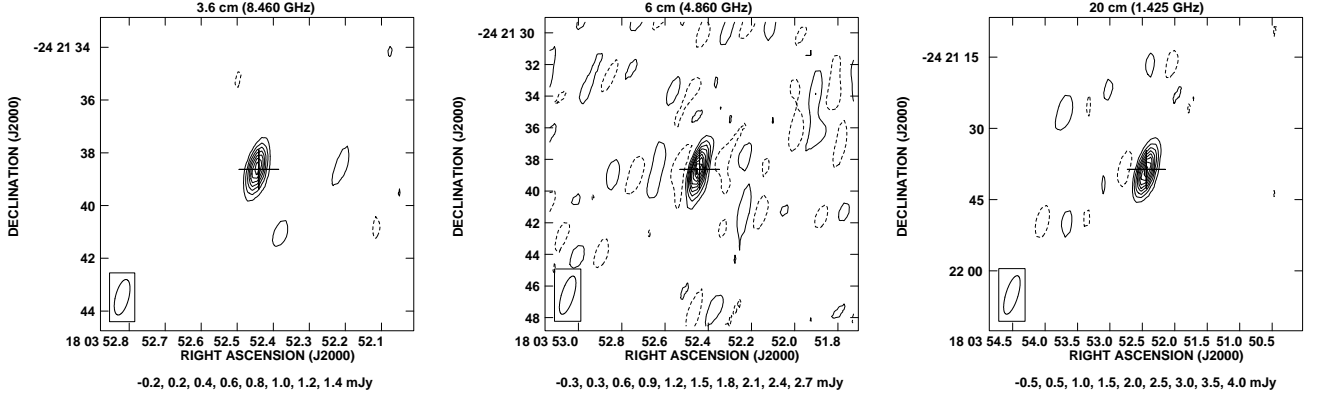


Fig. 7. Maps of 9 Sgr at 3.6, 6 and 20 cm (from left to right). Below each map the contour levels are listed. The negative contour is indicated by the dashed line. The crosses indicate the optical position (ICRS 2000.0) from the Simbad database. The beam sizes are $1.4'' \times 0.5''$ (position angle = 166°) at 3.6 cm, $2.5'' \times 0.8''$ (PA = 163°) at 6 cm and $8.4'' \times 2.6''$ (PA = 163°) at 20 cm. Note the different spatial scale for each of the maps.

This expression, adopted from Weber & Davis (1967), is valid only at large distances from the star ($r \geq 10 R_*$), which covers the region where the synchrotron radiation is emitted. We follow White (1985) in assuming $v_{\text{rot}} = 250 \text{ km s}^{-1}$. This value is plausible, as $v_{\text{rot}} \sin i = 128 \text{ km s}^{-1}$ (see Table 1). Free-free absorption in the wind is taken into account by setting the lower spatial boundary to the effective radius R_v of the radio emission (Wright & Barlow 1975).

Besides the power law in momentum space (with exponent n), we also assume a power law (with exponent δ) for the spatial dependence of the distribution:

$$N(p, r) = f_* n_e^* (n - 1) \left(\frac{p_0}{m_e c} \right)^{n-1} \left(\frac{r}{R_*} \right)^{-\delta} p^{-n} \quad (3)$$

where f_* and n_e^* are the fraction of relativistic electrons and the total electron number density at the stellar surface.

Equation (1) is to be integrated numerically. We take into account the Razin effect, due to the presence of a background plasma (Razin 1960). This effect causes synchrotron radiation to be suppressed at higher wavelengths.

5.2. Fitting the observations

We adopt the stellar parameters listed in Table 1. For the surface magnetic field we assume a value of $B_* = 100 \text{ Gauss}$ (Chen & White 1994). In Fig. 8 we present a model that fits our observations. We set $\delta = 1$, and then adapted n , f_* and R_{max} , which gives $n = 5.5$, $R_{\text{max}} = 160 R_*$ and $f_* = 4.5 \times 10^{-3}$. Of these parameters R_{max} appears to be the most critical. As expressed in

Table 9. A comparison of our radio flux determination with values from the literature (Florkowski et al. 1985; Bieging et al. 1989). Our error bars are dominated by the uncertainty in the background correction. The spectral indices derived from our data are also listed.

λ (cm)	Literature range flux (mJy)	Our data flux (mJy)	Spectral index
3.6		1.6 ± 0.4	-1.1 ± 0.6
6	$1.0(\pm 0.4) - 2.5(\pm 0.3)$	2.8 ± 0.4	-0.4 ± 0.3
20	$3.6(\pm 0.3) - 3.9(\pm 0.4)$	4.5 ± 1.2	

Eq. (1), R_{max} sets the outer boundary of the synchrotron emission region. It has been shown by CW91 that, due to the efficiency of Compton cooling, relativistic electrons cannot carry much of their energy out of the region where they are accelerated. Thus R_{max} can be interpreted as the position of the terminal shock. The index n is determined by the compression ratio χ of the shock: $n = (\chi + 2)/(\chi - 1)$. A value of $n = 5.5$ corresponds to weak shocks with a compression ratio of about 1.7.

Given the large number of parameters fitting a limited number of observations, the solution is not unique. For instance, a model with $\delta = 0.4$, $n = 4.5$, $R_{\text{max}} = 165 R_*$ and $f_* = 8.9 \times 10^{-6}$ fits the observations equally well.

At this stage, it is worth pointing out that R_{max} is substantially larger than the radius of the formation region of the Ne IX and O VII triplets. Although the VLA data tell us that the shocks that produce radio emission exist out to large distances, these shocks do not contribute a significant fraction of the thermal X-rays. Since the emission measure of the X-ray line emission

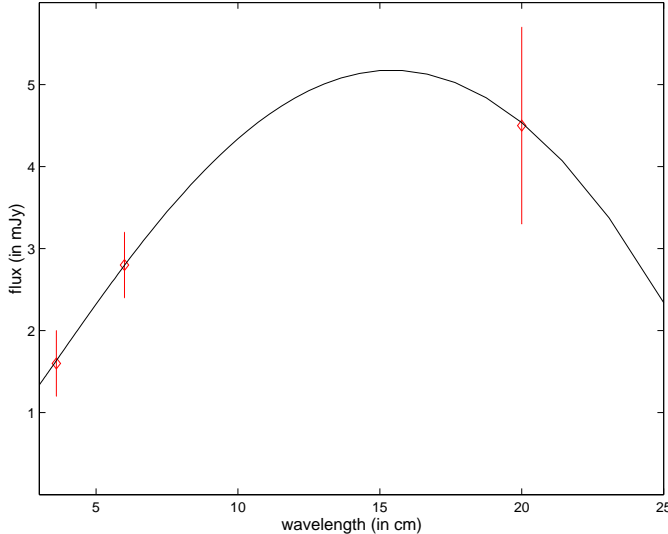


Fig. 8. Theoretical synchrotron radiation calculated with parameters $\delta = 1$, $n = 5.5$, $R_{\max} = 160 R_*$ and $f_* = 4.5 \times 10^{-3}$. The observations are displayed as open diamonds.

scales with the square of the density, the observed X-ray emission is dominated by the densest regions that lie outside the optical depth unity surface. The density in the outer shocks is obviously too low to compete with the emission from the shocks further in.

6. The optical spectrum

The optical spectrum of 9 Sgr displays a wealth of absorption lines from H_I, He_I, He_{II} as well as from some metal ions (e.g. O_{III}, C_{IV}, N_{III}, N_{IV}, N_V, ...). There are also a few narrow emission lines: N_{III} $\lambda\lambda 4634-41$, C_{III} $\lambda 5696$ and Si_{IV} $\lambda 4116$.

The equivalent width ratio of the He_I $\lambda 4471$ and He_{II} $\lambda 4542$ absorption lines ($W' = EW(4471)/EW(4542) = 0.19$) yields an O4 spectral type, while the strength of the He_{II} $\lambda 4686$ absorption ($EW = 0.75 \text{ \AA}$) suggests a main-sequence luminosity class. These classifications are in agreement with results published in the literature (e.g. Mathys 1988). The presence of Si_{IV} in emission in addition to the N_{III} emissions and He_{II} $\lambda 4686$ absorption indicates an O4 V ((f^+)) classification (see Walborn et al. 2002). The lack of any line at Si_{IV} $\lambda 4089$ is usually interpreted as the $\lambda 4089$ absorption and emission canceling each other (see Walborn 2001).

We found no significant line profile variability in our spectra of 9 Sgr. This is in agreement with the conclusions of Fullerton (1990) and Fullerton et al. (1996), who did not detect profile variability in the C_{IV} $\lambda 5801$ and He_I $\lambda 5876$ lines.

Garmany et al. (1980) investigated the multiplicity of 9 Sgr from a set of eleven photographic spectra with a dispersion of 16.9 \AA mm^{-1} . They concluded that 9 Sgr is probably single and that the variations of about 30 km s^{-1} they detected arise most likely in the atmosphere of the star.

We have measured the radial velocities (*RVs*) of the strongest absorption lines in our spectra of 9 Sgr. We then averaged the *RVs* of nine of them (He_{II} $\lambda\lambda 4200, 4542, 4686, 5412$; He_I $\lambda\lambda 4471, 5876$; C_{IV} $\lambda\lambda 5801, 5812$ and

O_{III} $\lambda 5592$). The results listed in Table 10 do not reveal any significant *RV* changes. The mean *RV* averaged over the entire data set amounts to $15.1 \pm 1.3 \text{ km s}^{-1}$. None of the individual lines displays a 1σ *RV* dispersion over our data set exceeding 3.8 km s^{-1} . We conclude therefore that our data are consistent with a constant *RV* in May 2000 and 2001.

However, our mean *RVs* of the C_{IV} $\lambda 5801$ ($\overline{RV} = 23.2 \pm 2.5 \text{ km s}^{-1}$), C_{IV} $\lambda 5812$ ($\overline{RV} = 15.9 \pm 2.5 \text{ km s}^{-1}$) and He_I $\lambda 5876$ ($\overline{RV} = 12.7 \pm 1.9 \text{ km s}^{-1}$) lines are about 42 km s^{-1} more positive than the values quoted by Fullerton (1990) and Fullerton et al. (1996)⁵. The data of Fullerton et al. were collected over seven consecutive nights in June 1986 with a spectral resolving power of $\sim 25\,000$ and their 1σ dispersions on the mean *RV* of individual lines are comparable to our values. Therefore, although the time scale of the *RV* variations of 9 Sgr is certainly poorly constrained, we conclude that *RV* variations probably occur on time scales of several months or most probably several years.

Both datasets (i.e. Fullerton's and ours) rule out *RV* variations on time-scales of a few days and probably up to several weeks. This is in stark contrast with the results of Garmany et al. (1980) who reported variations of 20 km s^{-1} within two days that they ascribed to the stellar wind. Given the low amplitude of the *RV* variations, only high-quality, high-resolution spectroscopic data are suited to probe the binarity of 9 Sgr and a long-term monitoring of this star is clearly required to unveil *RV* variations such as those occurring over relatively short time intervals around periastron passage in highly eccentric binaries.

Fullerton (1990) already suspected 9 Sgr to be a spectroscopic binary and pointed out that the mean profiles of both the C_{IV} and He_I absorptions were asymmetric, displaying a prominent extension towards their red wing (see his Fig. A133). We do not observe such an asymmetry in our data. The lack of this feature in our data could indicate that we are indeed seeing a long-period double-lined spectroscopic binary which was near conjunction in May 2000 and 2001, whereas it was near quadrature in June 1986.

7. Discussion

Let us start by summarizing the most important results of our multi-wavelength investigation of 9 Sgr. The present VLA data show that at the time of the *XMM-Newton* observation, the radio emission of 9 Sgr was definitely non-thermal and the level of emission was in the high end of the range hitherto observed for this star. Our EPIC spectra reveal a hard X-ray component that can be fitted equally well by a multi-temperature thermal model including some plasma at $kT \geq 1.46 \text{ keV}$ or by a rather steep power law ($\Gamma \geq 2.9$) component. Our RGS spectra of 9 Sgr seem consistent with the overall picture of X-ray emission due to shocks distributed throughout the stellar wind. Finally, our optical spectra indicate no *RV* variations on time

⁵ We can safely rule out that the velocity shift could be caused by wavelength calibration uncertainties. Indeed, our mean *RV* of the interstellar Na_I $\lambda 5890$ line ($-12.3 \pm 0.2 \text{ km s}^{-1}$) is in good agreement with the mean of Fullerton's (1990) data ($-13.4 \pm 0.2 \text{ km s}^{-1}$).

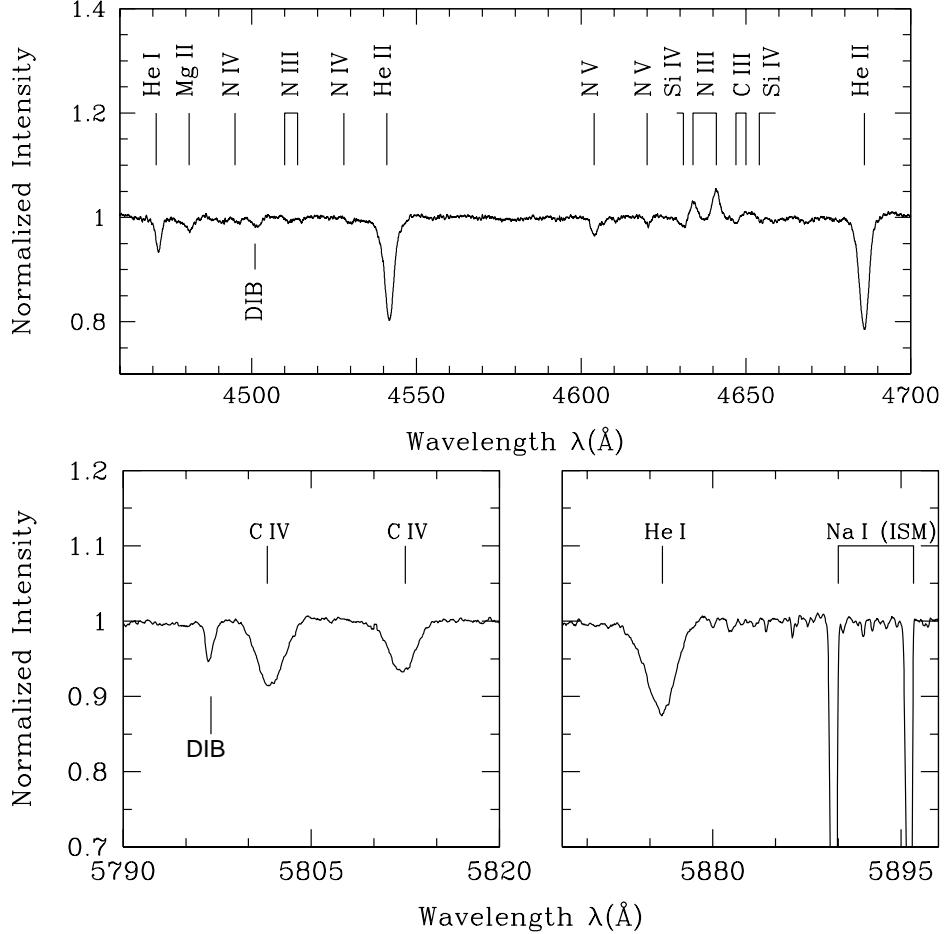


Fig. 9. Upper panel: FEROS spectrum of 9 Sgr in the blue wavelength range. Lower panel: average FEROS spectrum of 9 Sgr around the C IV $\lambda\lambda 5801, 5812$ lines and the He I $\lambda 5876$ line. Contrary to what happened in the data of Fullerton (1990), there is no outstanding asymmetry in the red wing of these line profiles.

scales of weeks but reveal a significant RV change compared to data taken fifteen years before.

7.1. Long term variability of the X-ray flux of 9 Sgr?

First, we briefly consider the issue of long term variability of the X-ray emission of 9 Sgr. 9 Sgr was observed at three occasions with the PSPC instrument onboard the *ROSAT* satellite. The observations took place between 1991 and 1993. We have extracted these observations from the archive and analysed them using the xSELECT software. The counts of 9 Sgr were extracted within a radius of $36''$ and the background was evaluated over an annulus around the source region. The background corrected count rates are provided in Table 11. These data do not provide evidence for strong variability of the X-ray flux. Note also that converting the best fitting parameters of the 1-T mekal + power law model discussed hereabove into the theoretical *ROSAT*-PSPC count rates yields 0.157 cts s^{-1} . Given the different sensitivities of the PSPC, EPIC and RGS instruments, this value is in pretty good agreement with the observed count rates. We conclude that the available data provide no indication of a strong variability of the soft X-ray flux of 9 Sgr.

Table 10. Radial velocities of 9 Sgr as measured on our FEROS data.

Date HJD – 2 450 000	\overline{RV} (km s^{-1})
1669.718	14.9
1670.703	17.6
1671.710	15.5
1672.691	15.8
2037.731	14.6
2039.934	13.6
2040.694	14.1

7.2. What is the distribution of relativistic electrons in the wind of 9 Sgr?

According to Bell (1978), a hydrodynamic shock with a compression ratio χ produces a population of relativistic electrons with energies following a power law distribution of index $n = (\chi + 2)/(\chi - 1)$. When these electrons undergo inverse Compton scattering, they produce a power law spectrum of photon index

Table 11. *ROSAT-PSPC* count rates of 9 Sgr as obtained from three pointings of the star.

Sequence number	Duration (s)	Date	PSPC rate (cts s ⁻¹)
rp200194n00	1638	17 Mar. 1991	.173 ± .012
rp201261n00	4500	4 Oct. 1992	.164 ± .006
rp900374n00	10432	1 Apr. 1993	.160 ± .004

$\Gamma = (n + 1)/2$ (CW91). In their model, CW91 consider a distribution of relativistic electrons with $n = 2$ (i.e. $\chi = 4$) resulting in a power law spectrum with photon index $\Gamma = 1.5$. Using the parameters from Table 1 and Eq. (33) from CW91, we would expect a flux of $\sim 10^{-5} \eta / B_*$ photons s⁻¹ cm⁻² at 1 keV, where η stands for the ratio of the electron acceleration efficiency to that of ions. This spectral shape is clearly at odds with our X-ray observations of 9 Sgr.

Our data provide the tightest constraints on the properties of a hard X-ray power law tail in an O-star so far. We note that the *EINSTEIN-SSS* observations of the Orion Belt stars that motivated the work of CW91 may have been affected by calibration issues involving the formation of ice on the entrance window of this instrument. Indeed, subsequent *ASCA* observations of δ Ori failed to confirm the existence of a hard power law tail in its X-ray spectrum (Corcoran et al. 1994).

Assuming that the $\Gamma \geq 2.9$ power law component in our spectral fits is indeed due to inverse Compton scattering by a population of relativistic electrons, we find that $n \geq 4.8$ and thus $\chi \leq 1.79$ are implied. It is interesting to note that our VLA data also suggest a low compression ratio of $\chi \simeq 1.7$. The latter ratios are much smaller than the strong shock value $\chi = 4$ used by CW91. Let us emphasize that the shocks responsible for the acceleration of the electrons that produce the synchrotron radio emission must be located at rather large radii. In fact, the surfaces of radial optical depth unity lie at 36, 53 and 125 R_* for emission at 3.6, 6 and 20 cm respectively (assuming a homogeneous, spherically symmetric, wind). On the other hand, hard X-rays can arise from very close to the stellar surface and it would thus not be too surprising to have different compression ratios for the different energy domains.

Our results suggest that if the hard X-ray emission in the spectrum of 9 Sgr is indeed due to a non-thermal phenomenon, then the acceleration of relativistic electrons in the atmosphere of this star cannot be described by the model of Chen & White (1991). The theory of CW91 is based on a number of assumptions on the shock properties which may need to be revised. The elaboration of such a model is beyond the scope of the present paper and we defer this work to a future paper.

At this stage, let us stress that the compression ratios we infer from the X-ray and radio data should be seen as typical or average values. Rather than having one definite compression ratio, the shocks in the wind are likely to have a distribution of compression ratios, as is also suggested by hydrodynamical models (e.g. Feldmeier et al. 1997). In this regard, it is natural that the values we find are lower than the maximum value of $\chi = 4$.

7.3. Is 9 Sgr a binary system?

Assuming instead that the high energy spectrum of 9 Sgr is of thermal origin, a possible explanation to account for the strong non-thermal radio emission and the lack of non-thermal X-rays is to imagine that the radio emission arises from electrons accelerated in a shock region far away from the photosphere of the O4 star where inverse Compton scattering would be less efficient. This could be the case if 9 Sgr were a binary system. As pointed out above, our data hint at a variation of the RV of 9 Sgr over time scales of months or probably years.

Abbott et al. (1984) suggested that non-thermal radio emission might arise from accretion onto an undetected compact companion in a so-called *X-ray quiet* binary system. However, as pointed out by these authors, the extreme youth of 9 Sgr (age ~ 1.5 Myr, Sung et al. 2000) argues against this hypothesis. In fact, even extremely massive stars of $120 M_\odot$ would not have the time to complete their evolution and end up as a compact object within 1.5 Myr (e.g. Maeder & Meynet 1994). However, 9 Sgr may be a post mass-exchange binary, in which the present-day primary was rejuvenated through mass accretion and mimics a younger age. This possibility cannot be fully discarded although one would probably expect some peculiar abundances in the photosphere of the star. The analysis of Bohannan et al. (1990) did not reveal evidence for such peculiar abundances.

Another mechanism to produce non-thermal radio emission in a binary system relies on the colliding wind scenario (Eichler & Usov 1993). Dougherty & Williams (2000) showed that seven out of nine non-thermal radio emitting Wolf-Rayet (WR) stars are visual or spectroscopic binaries. Therefore, these authors argue that most, if not all, of the Wolf-Rayet stars that display non-thermal radio emission could be colliding wind binaries. Could 9 Sgr be a colliding wind binary system then? Let us point out that the X-ray luminosity of 9 Sgr $L_X \simeq 1.4 \times 10^{33}$ erg s⁻¹ (corrected for an interstellar column of 0.22×10^{22} cm⁻² and assuming $d = 1.58$ kpc) is not exceptional for a star of this bolometric luminosity (e.g. Berghöfer et al. 1997). The ratio $\log(L_X/L_{\text{bol}}) = -6.35$ reveals no outstanding excess attributable to a wind interaction. In order to produce such a modest X-ray luminosity, a colliding wind binary would need to be either very wide (shocked winds adiabatic, see e.g. Pittard & Stevens 1997) or very close (winds collide before they accelerate to large velocities). The latter case can be ruled out because the wind collision region (and hence the electron acceleration site) would be located deep inside the opaque radio photosphere making it very difficult to observe any non-thermal radio emission. Also we would expect to observe substantial *RV* changes on time scales of a few days or weeks, unless the orbital inclination would be almost zero degrees. The possible long-term *RV* variations that we have uncovered suggest that this is not the case. Therefore, it seems more likely that 9 Sgr is a wide long-period spectroscopic binary.

If the asymmetry in the C IV and He I lines reported by Fullerton (1990) reveals indeed an SB2 binary at a phase near quadrature, then the companion of the O4 V star must be

another O-type star⁶. Of course more observations are needed to ascertain this scenario, but it is worth pointing out that the combined optical brightness of two main-sequence O-stars may lead to an interesting problem with the distance of 9 Sgr. Throughout this paper we have assumed a distance of 1.58 kpc, while Sung et al. (2000) derived $d = 1.78$ kpc for the NGC 6530 cluster. Therefore, it remains to be seen whether there is ‘enough room’ in the optical brightness of 9 Sgr for an O-type companion.

Mason et al. (1998) performed speckle observations of a sample of O-stars including 9 Sgr. The speckle camera used by these authors can detect binaries with angular separations in the range $0.035'' < \rho < 1.5''$ and with an optical brightness ratio of $\Delta m_V \leq 3$. Let us assume that the non-detection of a visual companion by Mason et al. allows us indeed to rule out the presence of a companion at more than $0.035''$. At a distance of 1.58 kpc, this corresponds to a linear separation of 55 AU. Now, assuming that 9 Sgr consists of an O4 V primary of mass $M \sim 55 M_\odot$ and an \sim O8 V secondary of $M \sim 25 M_\odot$, we find that the non-detection of Mason et al. (1998) sets an upper limit of 45 yrs on the orbital period of a binary seen at quadrature phase and assuming a circular orbit.

Could a wind-wind collision in a long-period binary produce the observed X-ray spectrum? Wide colliding wind systems have an adiabatic wind collision where the X-ray luminosity scales as the inverse of the orbital separation. Most wide systems (with orbital periods greater than one year) that we know about are WR + O binaries, and the higher mass-loss rate of the WR component helps to keep the X-ray emission fairly strong (e.g. WR 140). However, in an O + O binary, the X-ray luminosity should be drastically reduced (since L_X scales as \dot{M}^2 , Pittard & Stevens 1997). In an O + O binary with a period of a few years or more, one expects that the soft X-ray emission would remain dominated by the intrinsic emission from each star while the wind-wind collision would only dominate at high energies (e.g. $E > 3$ keV) where there is no contribution from intrinsic wind shocks. We have carried out hydrodynamic simulations (e.g. Pittard & Stevens 1997; Pittard 2000) of the X-ray emission of a colliding wind system consisting of an O4 primary ($\log \dot{M} = -5.6$, $v_\infty = 2950 \text{ km s}^{-1}$, $M = 55 M_\odot$) and an O8 secondary ($\log \dot{M} = -6.6$, $v_\infty = 2950 \text{ km s}^{-1}$, $M = 25 M_\odot$). For an assumed orbital period of 10 yrs (orbital separation 20 AU) the hydrodynamic model predicts a luminosity of $\sim 5 \times 10^{32} \text{ erg s}^{-1}$. The corresponding flux at 3 keV is $6.7 \times 10^{-14} \text{ erg cm}^{-2} \text{ s}^{-1} \text{ keV}^{-1}$ which is about a factor 3 too high compared to the observed flux of 9 Sgr. However, increasing the orbital separation by the same factor 3 would reduce the predicted flux to match the observed value, which would then imply an orbital period of approximately 50 yrs. It can also be seen that the simulated colliding wind spectrum (see Fig. 10) does not fall off as fast as the hard energy tail of the observed spectrum. Reducing the pre-shock wind velocity, particularly of the primary star, would reduce this discrepancy.

We note that confirming the presence of an iron K α line in future observations would suggest that the hard X-ray

continuum is thermal too and would lend further support to the colliding wind interpretation.

Finally, let us point out that among the seven non-thermal radio emitting O-type stars listed by Williams (1996), there are at least three confirmed binary or multiple systems (HD 15558, HD 167971 and Cyg OB2 No. 5). Cyg OB2 No. 5 consists of a short period colliding wind binary (Rauw et al. 1999) with a more distant third component. The non-thermal radio emission has been resolved with the VLA and has been suggested to be associated with the wind interaction zone between the short period binary and the third component (Contreras et al. 1997). HD 167971 (O8 Ib(f)p) has the strongest non-thermal radio emission among the OB stars detected in the survey of Bieging et al. (1989). Leitherer et al. (1987) describe HD 167971 as a close eclipsing O-star binary ($P_{\text{orb}} = 3.32$ days) with a third more distant and much brighter O8 I companion (which could be a line of sight object). HD 15558 is the spectroscopic O-star binary with the longest orbital period hitherto known ($P_{\text{orb}} = 439.3$ days, $e = 0.54$, Garmany & Massey 1981).

7.4. Conclusions and final remarks

Our multi-wavelength investigation of 9 Sgr confirms the non-thermal origin of its radio emission. However, the X-ray data do not reveal the $E^{-1.5}$ hard power law tail predicted by the model of CW91. Instead, we find that the X-ray spectra can be fitted if we include a steep power law component in the fits. If this model component is real, then the relativistic electrons that produce it must be accelerated in weak shocks with a very low compression ratio.

In this context, it is interesting to point out that Skinner et al. (2002) reported the existence of a hard X-ray component in the presumably single Wolf-Rayet star WR 110. This hard component could be either thermal ($kT \geq 3$ keV) or non-thermal emission. In the former case, Skinner et al. (2002) propose a model where the Wolf-Rayet wind crashes onto an as yet undetected close companion. In the latter case, the hard component can be fitted with a photon index $\Gamma = 2.2_{-0.3}^{+0.4}$, not too different from the theoretical value of CW91 corresponding to strong shocks. Skinner et al. caution that the radio emission from WR 110 yields no indication of a synchrotron component. However, the lack of non-thermal radio emission does not rule out the existence of a non-thermal X-ray emission since the synchrotron radio emission formed within the wind could be strongly absorbed by the huge free-free opacity. Therefore it could be that non-thermal X-ray emission is actually more common among early-type stars than expected from their radio properties. More observations of both thermal and non-thermal radio emitting early-type stars with *XMM-Newton* as well as the elaboration of new theoretical models are needed to clarify the nature of the hard X-ray emission component.

However, our optical data suggest that 9 Sgr could be a long-period spectroscopic binary. Therefore, it seems that a colliding wind scenario provides a plausible alternative and that the hard X-rays could be emitted in a very hot thermal plasma of a wind interaction region. A long-term high resolution spectroscopic monitoring of 9 Sgr is therefore indicated

⁶ The C IV lines are strongest at types O6 – O7 (Walborn 1980).

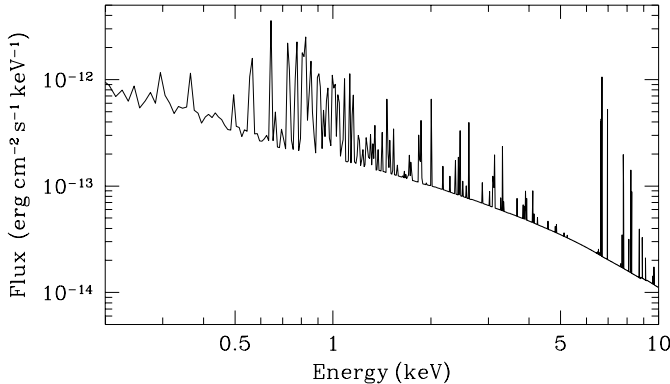


Fig. 10. Simulated unabsorbed X-ray emission from a wind-wind collision in an O4 + O8 binary system with orbital period 10 yrs. Interstellar and wind absorption would greatly reduce the flux below 1 keV, but the ISM column should only absorb a few per cent of the flux at 3 keV. See the text for details.

to unambiguously clarify the multiplicity of this star. Also it would be valuable to perform a multi-wavelength monitoring campaign to determine whether broad-band variations (like those seen in the radio, IR and X-rays for WR 140) can be established for 9 Sgr.

Acknowledgements. The authors wish to thank an anonymous referee for carefully reading our manuscript. We thank Dr. Yvan Stockman from the Centre Spatial de Liège (CSL) for useful information about the straylight behaviour of the *XMM-Newton* mirror modules. We are grateful to Dr. Barry Clark for kindly scheduling the VLA radio observation simultaneously with the *XMM* observation. Our thanks go also to Alain Detal (Liège) for his help in installing the sas and to Dr. Herman Hensberge (Royal Observatory of Belgium) for advising us in the reduction of the FEROS data. The Liège team acknowledges support from the Fonds National de la Recherche Scientifique (Belgium) and through the PRODEX XMM-OM and Integral Projects. This research is also supported in part by contracts P4/05 and P5/36 “Pôle d’Attraction Interuniversitaire” (OSTC-Belgium). WLW was supported in part by NASA contract # NAG 5-10113. MCR acknowledges support from ESA-Prodex project No. 13346/98/NL/VJ(ic). SVL acknowledges the financial support of the Belgian OSTC. JMP gratefully acknowledges funding from PPARC for a PDRA position. This research has made use of the SIMBAD database, operated at CDS, Strasbourg, France and NASA’s Astrophysics Data System Abstract Service.

References

Abbott, D. C., Bieging, J. H., & Churchwell, E. B. 1984, *ApJ*, 280, 671

Bell, A. R. 1978, *MNRAS*, 182, 147

Berghöfer, T. W., Schmitt, J. H. M. M., & Cassinelli, J. P. 1996, *A&AS*, 118, 481

Berghöfer, T. W., Schmitt, J. H. M. M., Danner, R., & Cassinelli, J. P. 1997, *A&A*, 322, 167

Bieging, J. H., Abbott, D. C., & Churchwell, E. B. 1989, *ApJ*, 340, 518

Bohannan, B., Voels, S. A., Hummer, D. G., & Abbott, D. C. 1990, *ApJ*, 365, 729

Briggs, D. S. 1995, Ph.D. Thesis, The New Mexico Institute of Mining and Technology, Socorro, New Mexico

Cassinelli, J. P., & Swank, J. H. 1983, *ApJ*, 271, 681

Cassinelli, J. P., Miller, N. A., Waldron, W. L., MacFarlane, J. J., & Cohen, D. H. 2001, *ApJ*, 554, L55

Chen, W., & White, R. L. 1991, *ApJ*, 366, 512 (CW91)

Chen, W., & White, R. L. 1994, *Ap&SS*, 221, 259

Conti, P. S., & Ebbets, D. 1977, *ApJ*, 213, 438

Contreras, M. E., Rodríguez, L. F., Tapia, M., et al. 1997, *ApJ*, 488, L153

Corcoran, M. F., Waldron, W. L., MacFarlane, J. J., et al. 1994, *ApJ*, 436, L95

Cornwell, T., & Braun, R. 1989, in *Synthesis Imaging in Radio Astronomy*, ed. R. A. Perley, F. R. Schwab, & A. H. Bridle, ASP Conf. Ser., 6, 167

den Herder, J. W., Brinkman, A. C., Kahn, S. M., et al. 2001, *A&A*, 365, L7

Diplas, A., & Savage, B. D. 1994, *ApJS*, 93, 211

Donati, J.-F., Wade, G. A., Babel, J., et al. 2001, *MNRAS*, 326, 1265

Donati, J.-F., Babel, J., Harries, T. J., Howarth, I. D., Petit, P., & Semel, M. 2002, *MNRAS*, 333, 55

Dougherty, S. M., & Williams, P. M. 2000, *MNRAS*, 319, 1005

Eichler, D., & Usov, V. 1993, *ApJ*, 402, 271

Feldmeier, A., Puls, J., & Pauldrach, A. W. A. 1997, *A&A*, 322, 878

Fermi, E. 1949, *Phys. Rev.*, 75, 1169

Florkowski, D. R., Johnston, K. J., Wade, C. M., & de Vegt, C. 1985, *AJ*, 90, 2381

Fullerton, A. W. 1990, Ph.D. Thesis, University of Toronto

Fullerton, A. W., Gies, D. R., & Bolton, C. T. 1996, *ApJS*, 103, 475

Garmany, C. D., Conti, P. S., & Massey, P. 1980, *ApJ*, 242, 1063

Garmany, C. D., & Massey, P. 1981, *PASP*, 93, 500

Jansen, F., Lumb, D., Altieri, B., et al. 2001, *A&A*, 365, L1

Kaastra, J. S. 1992, *An X-ray spectral code for optically thin plasmas, Internal SRON-Leiden Report*

Kaastra, J. S., Mewe, R., & Raassen, A. J. J. 2002, in *New Visions of the X-ray Universe in the XMM-Newton and Chandra Era*, ed. F. Jansen, ESA SP-488, in press

Kahn, S. M., Leutenegger, M. A., Cottam, J., et al. 2001, *A&A*, 365, L312

Kaufer, A., Stahl, O., Tubbesing, S., et al. 1999, *The Messenger*, 95, 8

Lamers, H. J. G. L. M., & Leitherer, C. 1993, *ApJ*, 412, 771

Leitherer, C., Forbes, D., Gilmore, A. C., et al. 1987, *A&A*, 185, 121

Maeder, A., & Meynet, G. 1994, *A&A*, 287, 803

Mason, B. D., Gies, D. R., Hartkopf, W. I., et al. 1998, *AJ*, 115, 821

Mathys, G. 1988, *A&AS*, 76, 427

Mathys, G. 1999, in *Proc. IAU Coll. 169, Variable and Non-spherical Stellar Winds in Luminous Hot Stars*, ed. B. Wolf, O. Stahl, & A. W. Fullerton, *Lect. Notes Phys.*, 523, 95

Mewe, R., Gronenschild, E. H. B. M., & van den Oord, G. H. J. 1985, *A&AS*, 62, 197

Owocki, S. P., & Cohen, D. H. 2001, *ApJ*, 559, 1108

Penny, L. R. 1996, *ApJ*, 463, 737

Perley, R. A., & Taylor, G. B. 1999, *The VLA Calibrator Manual* (<http://www.aoc.nrao.edu/~gtaylor/calib.html>)

Pittard, J. M. 2000, Ph.D. Thesis, The University of Birmingham, UK

Pittard, J. M., & Stevens, I. R. 1997, *MNRAS*, 292, 298

Porquet, D., Mewe, R., Dubau, J., Raassen, A. J. J., & Kaastra, J. S. 2001, *A&A*, 376, 1113

Rauw, G., Vreux, J.-M., & Bohannan, B. 1999, *ApJ*, 517, 416

Rauw, G., Blomme, R., Waldron, W. L., et al. 2002, in *New Visions of the X-ray Universe in the XMM-Newton and Chandra Era*, ed. F. Jansen, ESA SP-488, in press

Razin, V. A. 1960, *Radiophysica*, 3, 584

Rybicki, G. B., & Lightman, A. P. 1979, Radiative Processes in Astrophysics (John Wiley & Sons)

Schulz, N. S. 1999, *ApJ*, 511, 304

Shull, J. M., & van Steenberg, M. E. 1985, *ApJ*, 294, 599

Skinner, S. L., Zhekov, S. A., Güdel, M., & Schmutz, W. 2002, *ApJ*, 572, 477

Stockman, Y., Barzin, P., Hansen, H., et al. 1998, in Proceedings of the First XMM Workshop on Science with XMM held at Noordwijk, The Netherlands, ed. M. Dahlem (http://xmm.vilspa.esa.es/news/ws1/ws1_papers.html)

Strüder, L., Briel, U., Dennerl, K., et al. 2001, *A&A*, 365, L18

Sung, H., Chun, M.-Y., & Bessell, M. S. 2000, *AJ*, 120, 333

Torres, A. V. 1987, *ApJ*, 322, 949

Turner, M. J. L., Abbey, A., Arnaud, M., et al. 2001, *A&A*, 365, L27

Walborn, N. R. 1980, *ApJS*, 44, 535

Walborn, N. R. 2001, in *Eta Carinae and Other Mysterious Stars: The hidden opportunities of emission spectroscopy*, ed. T. R. Gull, S. Johansson, & K. Davidson, ASP Conf. Ser., 242, 217

Walborn, N. R., Howarth, I. D., Lennon, D. J., et al. 2002, *AJ*, 123, 2754

Waldron, W. L., Corcoran, M. F., Drake, S. A., & Smale, A. P. 1998, *ApJS*, 118, 217

Waldron, W. L., & Cassinelli, J. P. 2001, *ApJ*, 548, L45

Weber, E. J., & Davis, L. Jr. 1967, *ApJ*, 148, 217

White, R. L. 1985, *ApJ*, 289, 698

Williams, P. M. 1996, in *Radio Emission from the Stars and the Sun*, ed. A. R. Taylor, & J. M. Paredes, ASP Conf. Ser., 93, 15 (San Francisco)

Wright, A. E., & Barlow, M. J. 1975, *MNRAS*, 170, 41